Synthesis, structure, and electrochemical performance of magnesium-substituted lithium manganese orthosilicate cathode materials for lithium-ion batteries

R.J. Gummow [a,*], N. Sharma [b], V.K. Peterson [b], Y. He [a]

[a] *School of Engineering and Physical Sciences, James Cook University, Douglas, Queensland 4811, Australia*
[b] *The Bragg Institute, Australian Nuclear Science and Technology Organization, Locked Bag 2001, Kirrawee DC, NSW 2232, Australia*

ARTICLE INFO

ABSTRACT

Magnesium-substituted lithium manganese orthosilicate (Li_2MnSiO_4) cathode materials with a nominal composition of $Li_2Mg_xMn_{1-x}SiO_4$, for $x = 0.4$ and 0.5 are synthesized by a solid-state route, at 700 °C in argon. The samples are characterized using powder X-ray and neutron diffraction, scanning electron microscopy, and galvanostatic cell-cycling. Rietveld analyses of the powder X-ray and neutron diffraction data show the formation of a monoclinic $P2_1/n$ structure related to gamma lithium phosphate with no significant impurity peaks. This structure of the Mg-substituted samples is in contrast to the unsubstituted Li_2MnSiO_4 compound that has a $Pmn2_1$ structure when synthesized under the same conditions. Unit-cell volumes of the Mg-substituted materials are intermediate between those of the $P2_1/n$ structure of Li_2MnSiO_4 and the isostructural low-temperature form of Li_2MgSiO_4, indicating the formation of a solid solution. The Mg-substituted materials feature mixed Mg/Mn cation sites, although no evidence of Li/Mn, Li/Mg or Li/Mg/Mn mixed sites are found. The $Li_2Mg_xMn_{1-x}SiO_4$ cathodes show improved electrochemical performance over that reported for the unsubstituted Li_2MnSiO_4 $P2_1/n$ phase. The $Li_2Mg_xMn_{1-x}SiO_4$ cathode performance remains limited by its poor electronic properties and the large particle size of the solid-state synthesized products. Optimization of the synthesis conditions is likely to lead to enhanced electrochemical performance.

© 2011 Elsevier B.V. All rights reserved.

1. Introduction

Lithium-ion batteries are currently used in many applications ranging from power supplies for small portable devices to large-scale batteries for electric vehicles and stationary storage for the electricity grid. No single battery chemistry, however, has yet been identified that meets all the requirements for large-scale applications [1]. The capacity and charge/discharge cycling-performance of a battery are generally limited by the performance of the cathode material which also contributes approximately 40% to the price of a high-energy lithium-ion cell [2]. The development of new, low-cost, high-performance cathodes is, therefore, essential to enable lithium-ion battery technology to achieve its full market potential.

The lithium transition-metal orthosilicates, Li_2MSiO_4 (M = Fe, Mn, and Co), have been proposed as a new class of high-capacity lithium-ion battery cathode [3–6]. Li_2MnSiO_4 and Li_2CoSiO_4 may provide a high electrochemical-capacity if the transition-metal cation can be fully oxidized from M^{2+} to M^{4+}, resulting in capacities of 333 mAh g^{-1} for M = Mn and 325.5 mAh g^{-1} for M = Co. Li_2MnSiO_4 is, however, preferred to Li_2CoSiO_4 as Mn is non-toxic, naturally

abundant, and low cost. The stable covalent bonds in the SiO_4 structural units also promise good stability and safety for these materials when used in commercial cells. The development of Li_2MnSiO_4 as a cathode material for practical applications has been limited by its low electronic-conductivity, the difficulty in producing phase-pure samples, and its structural instability upon delithiation [7–10].

Li_2MnSiO_4 crystallizes in three different structural forms at atmospheric pressure which are related to the γ and β polymorphs of Li_3PO_4 [11]. Density functional theory (DFT) calculations have indicated that the monoclinic $P2_1/n$ structure, related to γ-Li_3PO_4, is the lowest stability form of Li_2MnSiO_4 and it can be prepared by high-temperature synthesis (900–1150 °C) [12,13]. The orthorhombic polymorphs, related to β-Li_3PO_4, with space groups $Pmnb$ and $Pmn2_1$, differ only slightly in their energetic stability according to DFT calculations, and this is confirmed by the experimental observation of phase mixtures in samples. Careful control of the calcination temperature enables the impurity phases to be minimized and an essentially pure $Pmn2_1$ phase material can be formed by sol–gel synthesis at 700 °C in He/H$_2$ [7].

The monoclinic $P2_1/n$ polymorph has a three-dimensional (3D) network of sites available for lithium-ion diffusion. The 3D $P2_1/n$ polymorph may offer a higher lithium-ion diffusion rate than the other two β-Li_3PO_4-related polymorphs, which feature a two-dimensional (2D) network [11]. The stabilization

* Corresponding author. Tel.: +61 7 47816223; fax: +61 7 47816788.
  E-mail address: rosalind.gummow@jcu.edu.au (R.J. Gummow).

and lower-temperature formation of the $P2_1/n$ structure offers the possibility for improved electrode kinetics and enhanced performance compared to the other Li_2MnSiO_4 polymorphs.

The electrochemically inactive Li_2MgSiO_4 crystallizes in the $P2_1/n$ space group when synthesized at low temperature and is isostructural with the $P2_1/n$ polymorph of Li_2MnSiO_4 [14]. The formation of a solid solution of the form $Li_2Mg_xMn_{1-x}SiO_4$ for $0 < x < 1$ is likely as the ionic radii of the Mg^{2+} and Mn^{2+} cations in tetrahedral co-ordination are similar [15], being 0.57 and 0.66 Å, respectively. Although the addition of Mg will reduce the capacity relative to the un-doped sample as Mg cannot be oxidized beyond the 2+ oxidation state, it may serve to stabilize the $P2_1/n$ structure and to improve the performance of the material as a cathode. In this study we report the synthesis of compounds with the nominal compositions $Li_2Mg_{0.5}Mn_{0.5}SiO_4$ and $Li_2Mg_{0.4}Mn_{0.6}SiO_4$ and their structural and electrochemical properties.

2. Experimental

Samples of $Li_2Mg_xMn_{1-x}SiO_4$ with $x = 0.4$ and 0.5 were synthesized by a solid-state route. Stoichiometric quantities of LiOH (Sigma–Aldrich, >98%), $MnCO_3$ (Sigma–Aldrich, >99.9%), SiO_2 (fumed, Sigma–Aldrich, 0.007 µm), and $Mg(OH)_2$ (nanopowder, Sigma–Aldrich, 99.9%) were milled with dry hexane in a vibratory ball-mill for 1 h. The mixed powders were heated in vacuum to 700 °C in a tube furnace to decompose the precursors. The sample was then re-ground using a mortar and pestle and then annealed in argon (Ultra-high purity argon, BOC gas) at 700 °C for a further 24–48 h. Sample powders were stored in an argon glovebox.

The synthesized powders were characterized by X-ray powder diffraction (XRPD) using a Panalytical X'pert Pro X-ray diffractometer with Cu Kα radiation. Neutron powder diffraction (NPD) data were collected using the high-resolution powder diffractometer, Echidna [16], at the Open Pool Australian Light-water (OPAL) reactor facility at the Australian Nuclear Science and Technology Organization (ANSTO). Data were collected at $\lambda = 1.62285(2)$ Å for 9 h in the 2θ range $14° \le 2\theta \le 154°$, with the wavelength determined using the NIST Al_2O_3 SRM 676. Samples were sealed in 6 mm diameter vanadium cans in an argon glovebox, before being transferred to the instrument where data were collected at ambient conditions. Rietveld refinements were carried out using the GSAS [17] software suite with the EXPGUI [18] interface.

Particle sizes were determined by analysis of scanning-electron microscope images obtained with a JEOL JSM-5410LV instrument. The elemental composition of the samples (lithium, manganese, and magnesium) was determined by Inductively Coupled Plasma-Atomic Emission Spectrometry (ICP-AES) using a Varian Liberty Series II instrument. Samples were digested in hydrofluoric acid prior to analysis. Si is lost in the digestion process and therefore could not be analyzed. Digestion of Mg-containing samples resulted in the formation of a small amount of an unidentified black, insoluble residue, which limited the accuracy of the elemental determinations. No such residue was found with samples containing no Mg.

Energy-Dispersive Spectroscopy (EDS) was performed on carbon-coated powder samples using an Electron-Probe Microanalyser (EPMA) to provide another determination of the Mg:Mn:Si ratios in the product phases. Elements with low atomic mass cannot accurately be analyzed on this instrument. It was therefore not possible to determine lithium or oxygen contents accurately.

To prepare electrodes for electrochemical characterization the sample powder was ball-milled with 20 wt.% Super C-65 carbon (Timcal) in a high-speed rotary mill at 560 rpm for 20 h under argon. The resulting carbon-coated particles were then mixed with polyvinylidene difluoride (PVDF, Sigma–Aldrich) dissolved in N-methyl pyrrolidenone (NMP, anhydrous, 99.5%, Sigma–Aldrich) in a ratio of 74:13:13. Cathodes were formed by coating the resulting slurry onto aluminum foil current-collectors, followed by drying in vacuum for 10 h at 120 °C and pressing with a hydraulic press at 15 MPa. Typical cathode masses were 1–2 mg with a surface area of 1.2 cm^2. Swagelok-type electrochemical test-cells were assembled in an argon glovebox. The electrolyte used was a solution of lithium hexafluorophosphate (battery grade, >99.9%, Aldrich) in a 1:1 mixture by volume of ethylene carbonate and dimethyl carbonate (99%, Sigma–Aldrich). The anode consisted of a 12 mm diameter disc of 0.7 mm thick lithium foil. The anode and cathode were separated by two discs of micro porous polypropylene separator film (Celgard) saturated with the electrolyte solution. Assembled cells were cycled galvanostatically using a battery analyzer (MTI Corporation). Current rates of 5 and 10 mA g^{-1} were used to assess the effect of current rate on electrode performance.

3. Results and discussion

3.1. Structural evaluation

In order to determine accurate structural parameters for the Mg-substituted phases examined in this work, highly crystalline samples were synthesized by solid-state synthesis without any carbonaceous additives. The Mg-substituted samples with nominal composition $Li_2Mg_{0.5}Mn_{0.5}SiO_4$ and $Li_2Mg_{0.4}Mn_{0.6}SiO_4$ prepared at 700 °C are white in colour.

Rietveld refinements of the structural models of the $Li_2Mg_xMn_{1-x}SiO_4$ samples with $x = 0.40$ and 0.50 were undertaken with XRPD and NPD data. The starting structural model used was that of Politaev et al. [13] for Li_2MnSiO_4, in monoclinic $P2_1/n$ space group with no Li/Mn site mixing. Partial substitution of Mg for Mn at the Mn site was applied in the model. A number of other structural permutations were modeled, including Mn at Li sites, Mg at Li sites, and Li at the Mn/Mg site. For both samples, the model that best fit the XRPD data was for Mg at the Mn site. NPD data provides greater sensitivity to Li relative to XRPD data and NPD data were collected to verify the structural model obtained using the XRPD data. The Rietveld-refined structural model derived from the XRPD data, with no Li/Mn/Mg cation mixing at Li or Mn/Mg sites, was used as the starting structural-model for refinement against the NPD data. Li has a relatively large neutron absorption cross-section (63.579 barn at $\lambda = 1.6215(1)$ Å [19]) and the Lobanov and Alte da Veiga absorption correction [17,20] was applied to the Rietveld model. Site-occupancy factors (SOFs) and atomic-displacement parameters (ADPs) were not refined simultaneously. The same methodology that was applied to the structural evaluation using the XRPD data was subsequently applied to the NPD data, using model constraints imposed by the elemental scattering contrast offered by neutron diffraction based on naturally-abundant isotopes. Rietveld refinement of the SOFs of the lithium sites, Li(1) and Li(2), lead to SOFs ≥ 1 on both sites with a deterioration in the statistics of the fits of where R_p increases by 0.08%, wR_p increases by 0.1%, R_F^2 increases by 1.61%, and χ^2 increased by 0.26 against NPD data. Placing Mg or Mn on the Li(3) and/or Li(2) site while allowing the SOFs to refine results also in deterioration in the statistics of the fit and an overall lithium content of less than 2. Placing the corresponding amount of lithium on the Mg/Mn site or introducing vacancies results in similar or worse fits. Therefore, the model with only lithium on the lithium sites and a mixed Mg/Mn site gave the best fit and was considered more likely to be correct.

Final Rietveld refinements of the structural models were performed with the combination of both XRPD and NPD datasets, referred to as a combined refinement [21,22]. Lattice parameters

Table 1
Crystallographic parameters of the $Li_2Mg_{0.5}Mn_{0.5}SiO_4$ and $Li_2Mg_{0.4}Mn_{0.6}SiO_4$ structural models determined from XRD and NPD data.

Atom	x	y	z	$U_{iso} \times 100/Å^2$	Site occupancy/%	BVS
$Li_2Mg_{0.5}Mn_{0.5}SiO_4$						
Mn(1)	0.5022(4)[b]	0.1661(2)[b]	0.3040(4)[b]	3.0(1)[b]	54.2(4)[a]	2.00
Mg(1)	0.5022(4)[b]	0.1661(2)[b]	0.3040(4)[b]	3.0(1)[b]	45.8(4)[a]	1.70
Si	0.2530(5)	0.4131(23)	0.3089(5)	1.37(8)	100	4.00
Li(1)	0.002(2)	0.159(1)	0.302(2)	1.2(2)	100	1.02
Li(2)	0.236(2)	0.073(1)	0.710(2)	3.0(3)	100	0.87
O(1)	0.2552(6)	0.4106(3)	0.6372(5)	1.40(9)	100	1.97
O(2)	0.2520(6)	0.5542(3)	0.2076(6)	1.49(9)	100	1.92
O(3)	0.0408(5)	0.3398(4)	0.2083(7)	1.8(1)	100	1.74
O(4)	0.4584(5)	0.3416(3)	0.2044(6)	1.19(9)	100	1.97
$Li_2Mg_{0.4}Mn_{0.6}SiO_4$						
Mn(1)	0.5043(4)[b]	0.1659(2)[b]	0.3037(4)[b]	2.5(1)[b]	62.4(5)[a]	1.97
Mg(1)	0.5043(4)[b]	0.1659(2)[b]	0.3037(4)[b]	2.5(1)[b]	37.6(5)[a]	1.68
Si	0.2520(5)	0.4135(3)	0.3096(6)	1.42(9)	100	4.00
Li(1)	0.006(2)	0.160(1)	0.300(2)	0.7(3)	100	1.01
Li(2)	0.239(2)	0.074(1)	0.710(2)	2.1(3)	100	0.86
O(1)	0.2556(7)	0.4113(3)	0.6349(6)	1.4(1)	100	2.01
O(2)	0.2521(7)	0.5537(3)	0.2078(7)	1.5(1)	100	1.90
O(3)	0.0402(6)	0.3391(4)	0.2091(7)	1.6(1)	100	1.74
O(4)	0.4581(6)	0.3414(4)	0.2034(7)	1.3(1)	100	1.93

Refined composition $Li_2Mg_{0.458(4)}Mn_{0.542(4)}SiO_4$ in space group $P2_1/n$. For NPD: $R_p = 3.52\%$, $wR_p = 4.43\%$, $R_F^2 = 5.87\%$; XRD: $R_p = 1.33\%$, $wR_p = 1.74\%$, $R_F^2 = 7.38\%$, and combined $R_p = 1.46\%$, $wR_p = 2.02\%$, and $\chi^2 = 1.29$, for 57 variables.

Refined composition $Li_2Mg_{0.376(5)}Mn_{0.624(5)}SiO_4$ in space group $P2_1/n$. For NPD: $R_p = 3.52\%$, $wR_p = 4.44\%$, $R_F^2 = 6.43\%$; XRD: $R_p = 1.27\%$, $wR_p = 1.65\%$, $R_F^2 = 5.66\%$, and combined $R_p = 1.38\%$, $wR_p = 1.89\%$, $\chi^2 = 1.23$, for 58 variables.

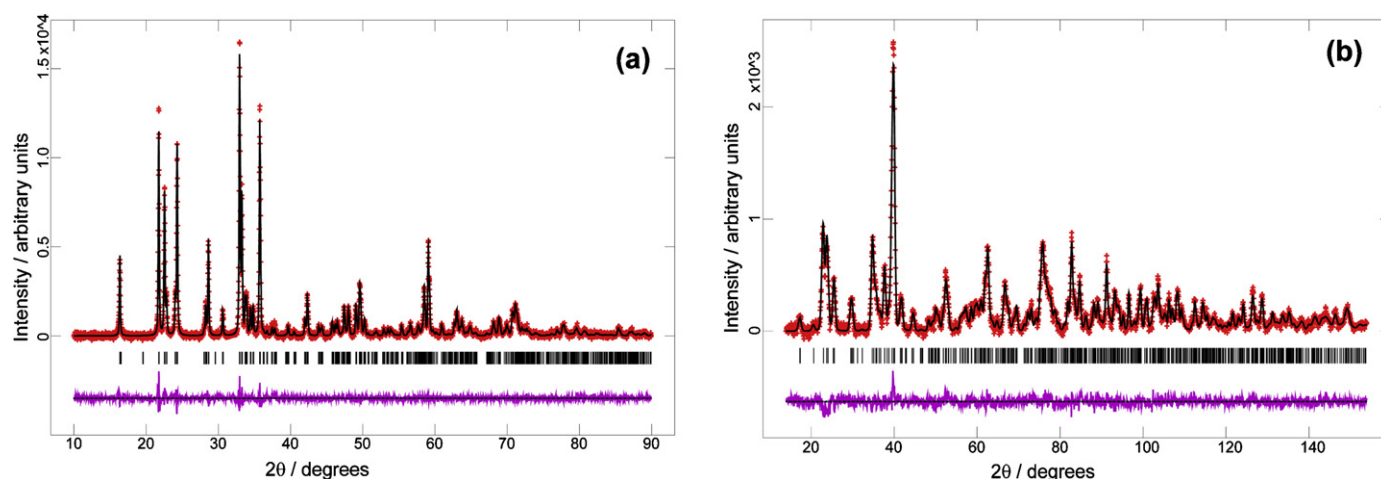[a] Constrained to total 100%.
[b] Constrained to be equal.

Fig. 1. The fit of the Rietveld-refined $Li_2Mg_{0.5}Mn_{0.5}SiO_4$ structural model to (a) XRD and (b) NPD data. Data are shown as crosses ($\times$), the calculated Rietveld model as a line through the data, the difference between the data and the model as a line below the data, and the Bragg-reflection markers as vertical lines. The statistics of the fits are (a) $R_p = 1.33\%$, $wR_p = 1.74\%$, $\chi^2 = 1.36$, and $R_F^2 = 5.87\%$, and (b) $R_p = 3.52\%$, $wR_p = 4.43\%$, $\chi^2 = 1.17$, and $R_F^2 = 7.38\%$. The combined parameters are given in the text.

and atomic parameters of the elements with larger X-ray scattering factors (e.g. Mg, Mn, and Si) were taken from the model derived from the XRPD data, and atomic parameters of the elements featuring better relative contrast between neutron-scattering lengths (e.g. Li and O) were taken from the model derived from the NPD data. The starting structural model of the combined refinement was refined against both datasets and therefore the reported structural model represents the least squares minimization of the residuals of the fits against both the NPD and the XRPD datasets. The crystallographic details of the models for $Li_2Mg_{0.5}Mn_{0.5}SiO_4$ and $Li_2Mg_{0.4}Mn_{0.6}SiO_4$ are presented in

Table 1, including calculated bond valence sums, BVS [23] and the figures of merit for the refinement, which are the profile factor (R_p), the weighted-profile factor (wR_p), the goodness-of-fit term (χ^2), and the Bragg R-factor (R_F^2). The XRPD and the NPD data together with the Rietveld-refined models are shown in Figs. 1 and 2, and their corresponding crystal structures are represented in Fig. 3. For $Li_2Mg_{0.5}Mn_{0.5}SiO_4$ the combined fit parameters are $R_p = 1.46\%$, $wR_p = 2.02\%$, and $\chi^2 = 1.29$, for 57 variables. For $Li_2Mg_{0.4}Mn_{0.6}SiO_4$ these parameters are $R_p = 1.38\%$, $wR_p = 1.89\%$, and $\chi^2 = 1.23$, for 58 variables. The refined compositions are $Li_2Mg_{0.46}Mn_{0.54}SiO_4$ and $Li_2Mg_{0.38}Mn_{0.62}SiO_4$, which are in good agreement with the

Table 2
Comparison of the chemical compositions of the $Li_2Mg_xMn_{1-x}SiO_4$ samples obtained from ICP, EDS, and Rietveld refinement using NPD and XRD data.

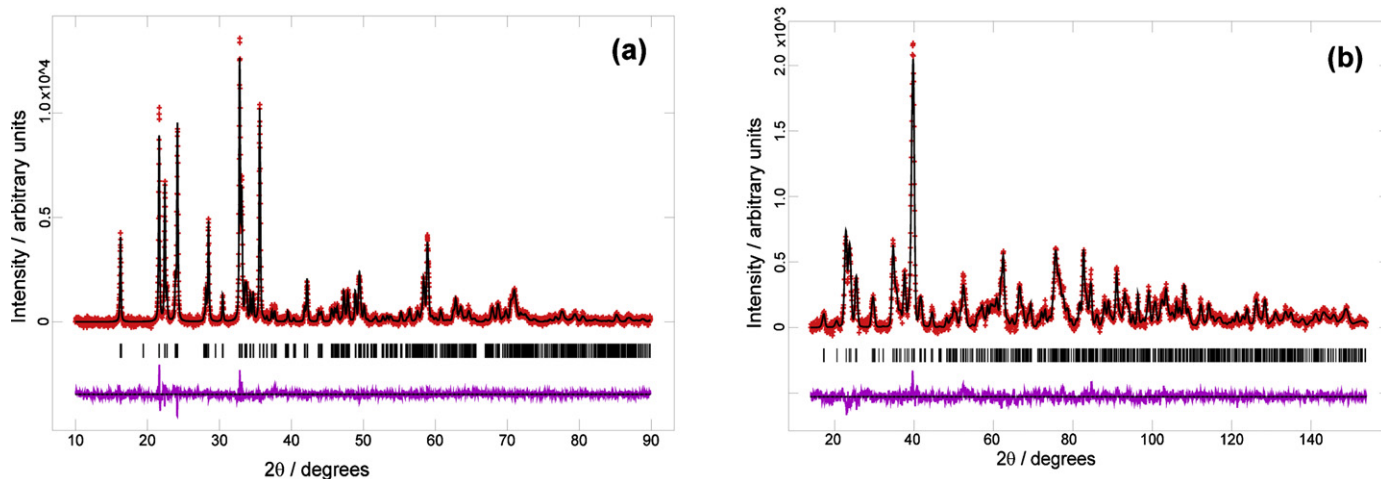| x	ICP Li:Mg	ICP Li:Mn	EDS Mg:Mn:Si	NPD and XRD Li:Mg:Mn
0.4	2:0.45	2:0.55	0.37:0.57:1	2:0.376(5):0.624(5)
0.5	2:0.52	2:0.55	0.49:0.55:1	2: 0.458(4):0.542(4)

Fig. 2. The fit of the Rietveld-refined $Li_2Mg_{0.4}Mn_{0.6}SiO_4$ structural model to (a) XRD and (b) NPD data. Data are shown as crosses ($\times$), the calculated Rietveld model as a line through the data, the difference between the data and model as a line below the data, and the Bragg-reflection markers as vertical lines. The statistics of the fits are (a) $R_p = 1.27\%$, $wR_p = 1.65\%$, $\chi^2 = 1.33$, and $R_F^2 = 6.43\%$, and (b) $R_p = 3.52\%$, $wR_p = 4.44\%$, $\chi^2 = 1.06$, and $R_F^2 = 5.66\%$. The combined parameters are given in the text.

Table 3
The refined lattice parameters and unit-cell volumes of the $Li_2Mg_xMn_{1-x}SiO_4$ samples compared with the end members Li_2MnSiO_4 ($x=0$) and Li_2MgSiO_4 ($x=1$).

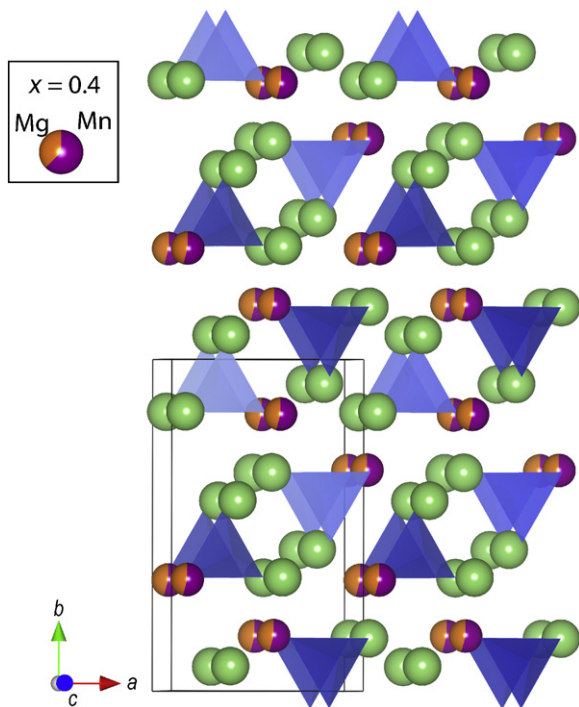| x	$a/\text{Å}$	$b/\text{Å}$	$c/\text{Å}$	β	Unit-cell volume/Å^3
0 [13]	6.3344(4)	10.9108(7)	5.0703(4)	90.990	350.8
0.4	6.3214(2)	10.8283(3)	5.0448(1)	90.750(2)	345.29(2)
0.5	6.3191(1)	10.8133(2)	5.0394(1)	90.7194(2)	344.32(2)
1 [14]	6.300(0)	10.692(2)	4.995(5)	90.47(1)	336.5

Fig. 3. The crystal structure of the sample of nominal composition $Li_2Mg_{0.5}Mn_{0.5}SiO_4$ with SiO_4 shown in blue, Li as green, Mn as purple, and Mg as orange. The shading on the spheres indicates the SOFs. Crystal axes are shown inset at the bottom left and indicate orientation. The inset at the top left shows the SOFs of the mixed Mg/Mn site in $Li_2Mg_{0.4}Mn_{0.6}SiO_4$ ($x=0.4$). (For interpretation of the references to color in this figure legend, the reader is referred to the web version of the article.)

synthetic input compositions and the elemental analysis results from EDS and ICP-AES (Table 2). The refined lattice-parameters and unit-cell volumes for the $Li_2Mg_xMn_{1-x}SiO_4$ samples, and the literature values for the $P2_1/n$ phases Li_2MnSiO_4 ($x=0$) and Li_2MgSiO_4 ($x=1$), are given in Table 3. Mg^{2+} has a smaller ionic radius than Mn^{2+} and therefore a reduction in the unit-cell volume is consistent with increasing Mg content. The data in Table 3 and Fig. 4 show that there is a linear relationship between the unit-cell volumes of the $Li_2Mg_xMn_{1-x}SiO_4$ phases and their Mg content. This is consistent with Vegard's law, confirming the formation of a solid solution.

The major finding of this work is that substitution of Mn by Mg to form compounds of nominal composition $Li_2Mg_xMn_{1-x}SiO_4$ with $x=0.40$ and 0.50 leads to stabilization of the $P2_1/n$ phase, even at the relatively low synthesis temperature of 700 °C. This is in sharp contrast to the unsubstituted Li_2MnSiO_4 compound which crystallizes in the $Pmn2_1$ space group when synthesized under similar conditions [9]. The two previous reports of the synthesis of the $P2_1/n$ form of Li_2MnSiO_4 both note that temperatures
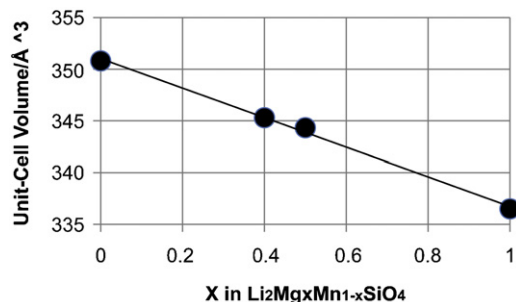

Fig. 4. Unit-cell volume of $Li_2Mg_xMn_{1-x}SiO_4$ as a function of the magnesium content.

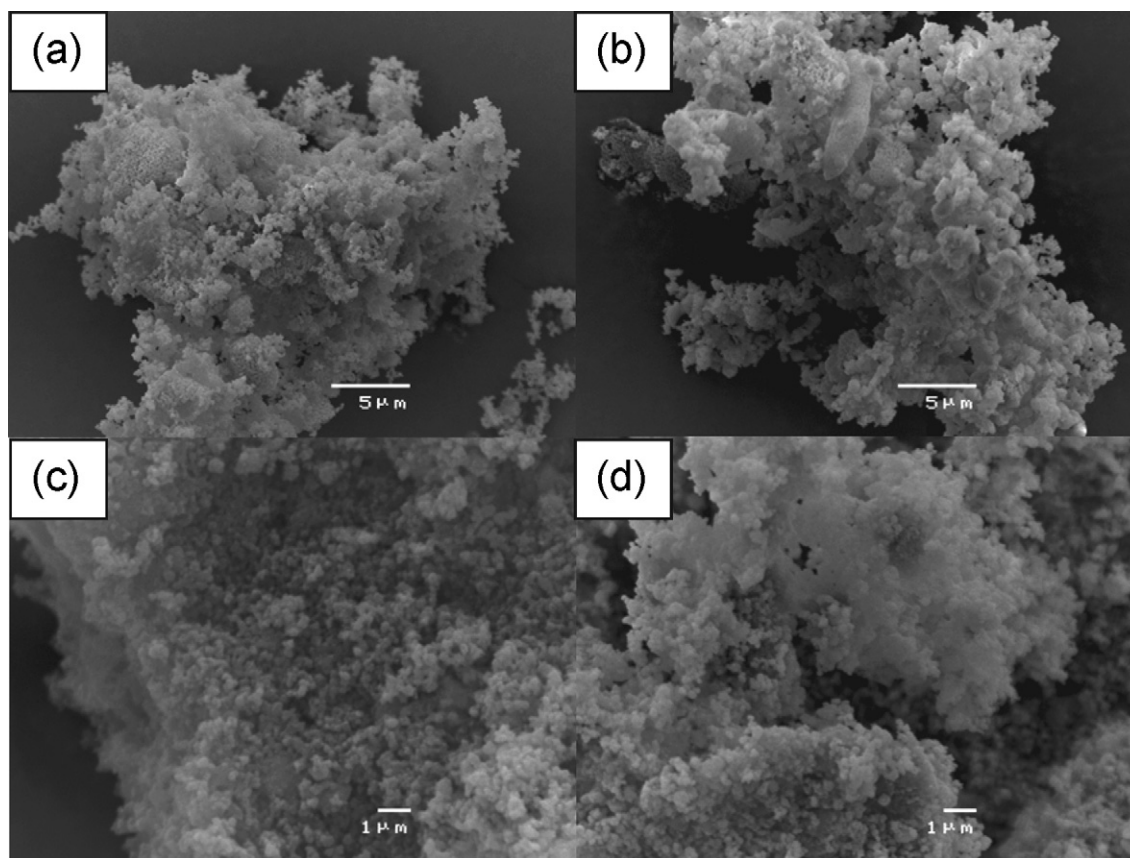**Fig. 5.** Scanning-electron microscope images of as synthesized (a) $Li_2Mg_{0.5}Mn_{0.5}SiO_4$ and (b) $Li_2Mg_{0.4}Mn_{0.6}SiO_4$ and ball-milled (c) $Li_2Mg_{0.5}Mn_{0.5}SiO_4$ and (d) $Li_2Mg_{0.4}Mn_{0.6}SiO_4$.

above 900 °C were required to crystallize this phase. Politaev et al. [13] synthesized a single-phase $P2_1/n$ polymorph of Li_2MnSiO_4 by calcination at 1150 °C in a hydrogen atmosphere. Subsequently, Mali et al. [12] prepared the $P2_1/n$ form with a minor Mn_2SiO_4 content, by heat-treatment of a sample with space group $Pmn2_1$, prepared by conventional hydrothermal synthesis, at 900 °C for 6 h in an argon atmosphere followed by rapid quenching to room temperature.

Rietveld analysis results from this study show no evidence for significant Li-ion vacancies, Li at the Mn/Mg-site, and Mn or Mg at any of the Li-sites. Therefore, unlike the structural model of Li_2MnSiO_4 proposed by Politaev et al. [13] which contains mixed Li/Mn sites, we observe no Li/M site mixing where M = Mg or Mn. The only cation mixing present is Mg/Mn at the Mg/Mn site. It is postulated that the presence of the Mg cation inhibits Li/Mn or Li/Mg site mixing. The presence of Mg/Mn cations at Li sites is undesirable as these large cations impede the diffusion of the Li ions through the lattice and cause deterioration in the electrochemical properties of the cathode.

3.2. Morphology

Scanning-electron microscopy (SEM) was used to determine the morphology of the samples. The SEM images of $Li_2Mg_{0.5}Mn_{0.5}SiO_4$ and $Li_2Mg_{0.4}Mn_{0.6}SiO_4$ after synthesis show large particles that consist of agglomerated smaller particles that have fused together during calcination (Fig. 5a and b, respectively). In the case of materials like Li_2MnSiO_4 and its derivatives, which have a low electronic and ionic conductivity, the products of solid-state synthesis do not have favorable morphology for electrochemical testing even when synthesized at the relatively low temperature

of 700 °C. The performance of such materials can be enhanced by forming an intimate mixture with carbonaceous additives. One approach to include carbon is through high energy ball-milling, which acts to reduce the particle size and to provide a carbon coating. An alternative method is to include a carbon-containing precursor in the solid-state synthesis, for example adipic acid or cellulose, which forms a carbon coating on the particles during their synthesis without the need for further reaction. In the present study the samples were milled for 20 h in a high energy ball-mill with 20 wt.% Super C-65 carbon. The SEM images of the samples after ball-milling show separated nanoparticles of approximately 200 nm diameter (Fig. 5c and d). The XRPD patterns of the samples after milling (Fig. 6) show no change in the bulk crystal-structure as a result of the milling process, however, peaks are broadened relative to the un-milled samples, consistent with a decrease in crystallite size and/or a slight loss in long-range structural order.

3.3. Electrochemical evaluation

The theoretical charge capacities for $Li_2Mg_xMn_{1-x}SiO_4$ electrodes with x = 0, 0.4, and 0.5 when charged to a manganese oxidation state of 3+ and 4+, respectively, are given in Table 4.

Table 4
Theoretical charge capacities of $Li_2Mg_xMn_{1-x}SiO_4$ samples.

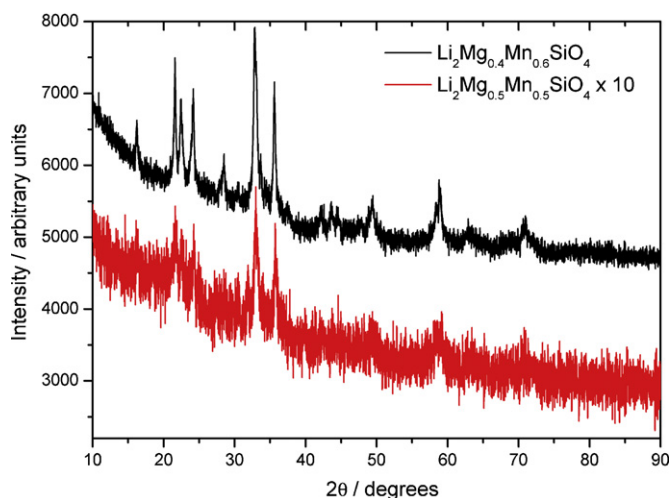| x	Capacity when charged to Mn^{3+}/mAh g^{-1}	Capacity when charged to Mn^{4+}/mAh g^{-1}
0	166	333
0.4	108	216
0.5	92	184

Fig. 6. X-ray powder diffraction data of ball-milled samples of $Li_2Mg_{0.5}Mn_{0.5}SiO_4$ (lower pattern) and $Li_2Mg_{0.4}Mn_{0.6}SiO_4$ (upper pattern).

Since the magnesium is electrochemically inactive, an increase in the magnesium content results in a reduction in the theoretical capacity and an increase in the residual lithium content of, the fully charged cathodes. For example, the fully charged composition of $Li_2Mg_{0.4}Mn_{0.6}SiO_4$ is $Li_{0.8}Mg_{0.4}Mn_{0.6}SiO_4$.

Fig. 7a and b shows the first five electrochemical cycles for a $Li/Li_2Mg_{0.5}Mn_{0.5}SiO_4$ (milled) cell at current rates of 5 and $10\,mA\,g^{-1}$, respectively. The capacity on the first charge cycle at the current rate of $5\,mA\,g^{-1}$ is $95\,mAh\,g^{-1}$ (Fig. 7a), in good agreement with the theoretical charge-capacity for oxidation of the manganese cations to the 3+ state (Table 4), corresponding to the removal of 0.5 lithium per formula unit. In this case the 3+/4+ redox couple of the manganese cations is not accessible below the cut-off voltage of 4.8 V. On the first discharge-cycle the capacity is only $62\,mAh\,g^{-1}$ corresponding to the re-insertion of 0.32 lithium ions per formula unit. It is, however, possible that some of the capacity measured for the charge cycles may arise from electrolyte decomposition reactions that occur at the high voltages reached. The irreversibility in the capacity between the charge and discharge cycles is consistent with charge capacity that is partially due to electrolyte decomposition rather than only lithium extraction.

At the higher current-rate (Fig. 7b) the polarization increases, resulting in a capacity of $56\,mAh\,g^{-1}$ on the first charge cycle. This
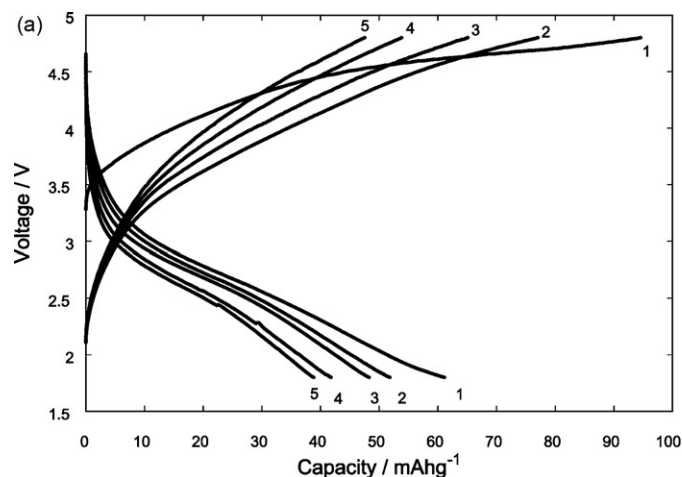
is significantly less than that obtained at the lower current-rate and corresponds to the removal of 0.3 lithium ions per formula unit, reflecting the relatively poor electronic conductivity of the cathode. Despite the carbon coating of the cathode, achieved by mechanical milling which also results in a reduction of the crystallite size, this low electronic conductivity remains a limiting factor for achieving good electrochemical performance of the cathode material.

After the initial charge there is a change in the shape of the charge curves, consistent with reported results for the $Pmn2_1$ phase of Li_2MnSiO_4. The change in shape of the charge curves is attributed to a structural re-arrangement of the Li and Mn cations in the lattice after the initial extraction of lithium [8,9]. Despite the presence of the Mg cations and the $P2_1/n$ structure, it appears that the crystal structure is modified during the electrochemical extraction of lithium cations. On cycling there is a 33% drop in the discharge capacity in the first 5 cycles at $5\,mA\,g^{-1}$ (Fig. 7a) and a 29% drop at $10\,mAh\,g^{-1}$ (Fig. 7b). Despite our expectations of improved cycling-performance for the Mg-substituted cathodes, we observe rapid capacity-fade upon cycling. Detailed structural studies of delithiated cathode materials, which are beyond the scope of the current investigation, are required to completely understand the link between structure and cycling and determine the reasons for the poor capacity-retention of the cathode. By analogy with the findings for materials with the orthorhombic $Pmn2_1$ structure, studied by other investigators, it is possible to speculate on the cause of the capacity fade. $Pmn2_1$ materials have been found to lose crystallinity upon cycling, resulting in a collapse of the crystal structure and an amorphization of the cathode after several cycles [3,10,24]. It is likely that a similar mechanism is occurring in this case which would account for the rapid loss in capacity.

Fig. 8 shows the first five cycles for a $Li/Li_2Mg_{0.4}Mn_{0.6}SiO_4$ (milled) cell. On the first charge cycle the sample with a nominal 40% magnesium at the M site shows a larger polarization than that for the cathode material containing a nominal 50% magnesium at the M site (Fig. 7a), with most of the capacity observed above 4.6 V. The capacity on the first charge is $96\,mAh\,g^{-1}$, similar to that found for the sample containing a nominal 50% magnesium at the M site. Similarly, a large irreversibility of the capacity on the first cycle is noted, suggesting (as with the cathode with a nominal 50% magnesium on the M site) that a proportion of the observed charge-capacity arises from electrolyte decomposition when charging to the upper cut-off voltage of 4.8 V. The capacity retention is poor with a rapid drop in capacity observed with cycling. Again, structural analyses of delithiated cathode materials are required to determine the capacity-fade mechanism and this will be explored in future work. We speculate that the rapid
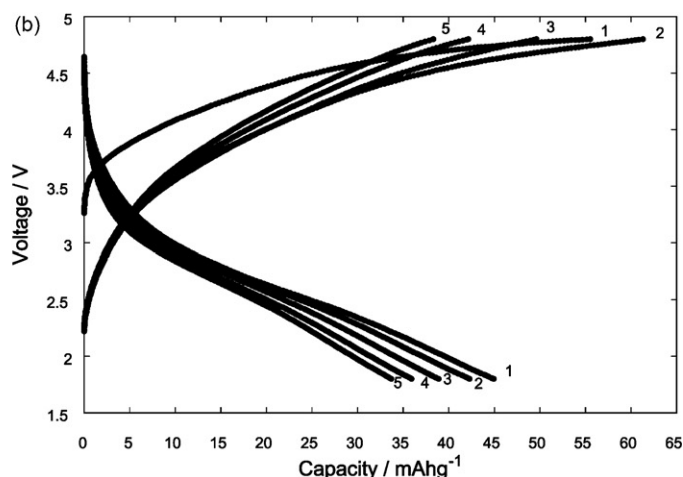

Fig. 7. Galvanostatic cycling curves for a $Li/Li_2Mg_{0.5}Mn_{0.5}SiO_4$ (milled) cell for cycles 1–5 at a current density of (a) $5\,mA\,g^{-1}$ and (b) $10\,mA\,g^{-1}$.
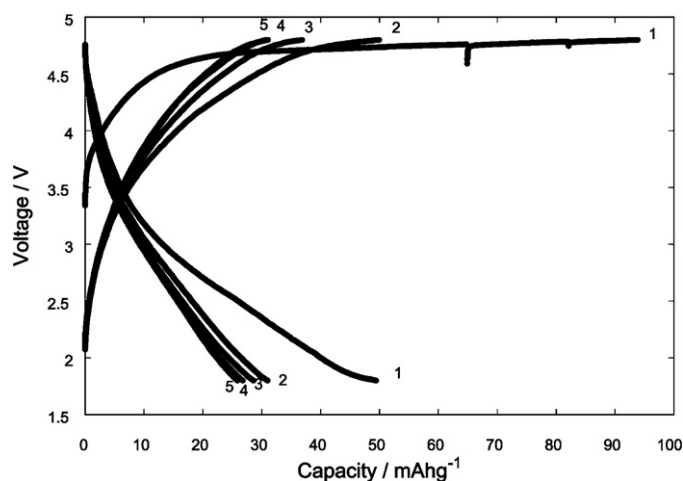
Fig. 8. Galvanostatic cycling curves for a Li/Li$_2$Mg$_{0.4}$Mn$_{0.6}$SiO$_4$ (milled) cell for cycles 1–5 at a current density of 5 mA g^{-1}.

capacity-fade is probably due to a loss of crystallinity of the cathode as discussed for the sample containing a nominal 50% Mg at the *M* site. The electrolyte decomposition reactions may also result in the formation of high-impedance surface layers on the electrode, which inhibit electrochemical activity.

Although the electrochemical performance of the cathode materials prepared in this study is relatively poor, there is a significant improvement compared to that of monoclinic Li$_2$MnSiO$_4$ reported by Politaev et al. [13]. Politaev et al. found high polarization on charge and limited electrochemical activity for the monoclinic cathode material, with only 4% of lithium atoms per formula unit extracted from the sample between 3.5 and 5 V against lithium metal, even when using a low current-density of 0.05 mA cm^{-2}. On discharge the voltage was reported to drop rapidly below 1.7 V. These relatively poor performance results are expected considering the high synthesis temperature for the sample (1150 °C). No data on the morphology of the sample was reported, but high synthesis temperatures generally result in larger average particle-sizes, which combined with the relatively poor conductivity of the material, limit the electrochemical activity as a consequence of the electrical isolation of the interior of the particles. Additionally, a small but significant amount of lithium was found on the Mn sites in the *P*2$_1$/*n* Li$_2$MnSiO$_4$ structural model [13]. In the present study of Mg-substituted samples, no significant Mg or Mn content is found at the lithium sites. In the Mg-doped samples, therefore, there are no large cations present along the lithium-diffusion channels, allowing for the unhindered diffusion of lithium ions.

Higher discharge-capacities have been reported for Li$_2$MnSiO$_4$ cathodes in studies by other investigators [5,7,8,10,25]. In all these studies, however, the crystal structure of the electrode has been the orthorhombic *Pmn*2$_1$ structure and not the monoclinic *P*2$_1$/*n* structure found for the materials in this study. This monoclinic structure differs from the orthorhombic structure in that it offers a three-dimensional framework through which the lithium ions can move compared to the two-dimensional orthorhombic structures. It is acknowledged that the electrochemical results are not optimal because of the solid-state synthesis technique which produces relatively large particles compared to other preparation techniques. The cathode material of this study was prepared specifically for diffraction experiments, which require larger particle sizes than materials that give optimal electrochemical performance.

4. Conclusions

In this study our results indicate that partial substitution of Mg for Mn in Li$_2$MnSiO$_4$ effectively stabilizes the *P*2$_1$/*n*

polymorph, enabling it to form at 700 °C. Single-phase compounds with nominal composition Li$_2$Mg$_x$Mn$_{1-x}$SiO$_4$ with $x = 0.4$ and 0.5 have been synthesized. Refinement of structural models with powder X-ray and neutron powder diffraction data confirms that these compounds crystallize with the *P*2$_1$/*n* space group when calcined at 700 °C. This is in contrast to unsubstituted Li$_2$MnSiO$_4$, for which the *P*2$_1$/*n* structure can only be synthesized above 900 °C [11,13].

Although the electrochemical performance of this cathode material is not ideal, our results demonstrate a new strategy for the possible stabilization of Li$_2$MnSiO$_4$ cathode structures that may lead to improved electrochemical properties. Further studies are underway to examine the compositional range of Mg-containing Li$_2$MnSiO$_4$ structures that can be synthesized and the potential for other cation dopants, of similar atomic radius to Mg, to stabilize crystal forms in this system. As found for unsubstituted Li$_2$MnSiO$_4$ [7,8,25], alternative synthetic techniques incorporating carbonaceous additives are likely to result in composite Mg-substituted materials with reduced particle-size and increased electronic conductivity, leading to enhanced electrochemical performance of these materials in practical cells.

References

[1] A. Manthiram, J. Phys. Chem. Lett. 2 (2011) 176–184.
[2] C. Daniel, JOM 60 (9) (2008) 43–48.
[3] R. Dominko, J. Power Sources 184 (2008) 462–468.
[4] R. Dominko, M. Bele, M. Gaberscek, A. Meden, M. Remskar, J. Jamnik, Electrochem. Commun. 8 (2006) 217–222.
[5] R. Dominko, M. Bele, A. Kokalj, M. Gaberscek, J. Jamnik, J. Power Sources 174 (2007) 457–461.
[6] C. Lyness, B. Delobel, A.R. Armstrong, P.G. Bruce, Chem. Commun. (2007) 4890–4892.
[7] I. Belharouak, A. Abouimrane, K. Amine, J. Phys. Chem. C 113 (2009) 20733–20737.
[8] C. Deng, S. Zhang, B.L. Fu, S.Y. Yang, L. Ma, Mater. Chem. Phys. 120 (2010) 14–17.
[9] W.G. Liu, Y.H. Xu, R. Yang, J. Alloys Compd. 480 (2009) L1–L4.
[10] W.G. Liu, Y.H. Xu, R. Yang, Rare Metals 29 (2010) 511–514.
[11] M.E. Arroyo-DeDompablo, R. Dominko, J.M. Gallardo-Amores, L. Dupont, G. Mali, H. Ehrenberg, J. Jamnik, E. Moran, Chem. Mater. 20 (2008) 5574–5584.
[12] G. Mali, A. Meden, R. Dominko, Chem. Commun. 46 (2010) 3306–3308.
[13] V.V. Politaev, A.A. Petrenko, V.B. Nalbandyan, B.S. Medvedev, E.S. Shvetsova, J. Solid State Chem. 180 (2007) 1045–1050.
[14] C. Jousseaume, A. Kahn-Harari, D. Vivien, J. Derouet, F. Ribot, F. Villain, J. Mater. Chem. 12 (2002) 1525–1529.
[15] R.D. Shannon, C.T. Prewitt, J. Inorg. Nucl. Chem. 32 (1970) 1427–1441.
[16] K.D. Liss, B. Hunter, M. Hagen, T. Noakes, S. Kennedy, Phys. B: Condens. Matter 385–86 (2006) 1010–1012.
[17] A.C. Larson, R.B. Von Dreele, Los Alamos National Laboratory Report LAUR (1994) 86748.
[18] B.H. Toby, J. Appl. Crystallogr. 34 (2001) 210–213.
[19] V.F. Sears, Neutron News 3 (1992) 29.
[20] N.N. Lobanov, L.A.d. Veiga, Presented at the Sixth European Powder Diffraction Conference, August 22–25, 1998.
[21] N. Sharma, R.L. Withers, K.S. Knight, C.D. Ling, J. Solid State Chem. 182 (2009) 2468–2474.
[22] N. Sharma, R.B. Macquart, M.M. Avdeev, M. Christensen, G.I. McIntyre, Y.-S. Chen, C.D. Ling, Acta Crystallogr. B 66 (2010) 165–172.
[23] N.E. Brese, M. O'Keeffe, Acta Crystallogr. B 47 (1991) 192–197.
[24] A. Kokalj, R. Dominko, G. Mali, A. Meden, M. Gaberscek, J. Jamnik, Chem. Mater. 19 (2007) 3633–3640.
[25] Y.-X. Li, Z.-L. Gong, Y. Yang, J. Power Sources 174 (2007) 528–532.